International Journal of Nanomedicine

Dovepress

open access to scientific and medical research

Open Access Full Text Article

ORIGINAL RESEARCH

Procedural Promotion of Multiple Stages in the Wound Healing Process by Graphene-Spiky Silica Heterostructured Nanoparticles

Jie Li[1], Jiangtao Long[1], Zheng Zhao[2], Qianqian Wang[1], Wang Bo[2], Liang Ren[1], Yan Fan[3], Peng Wang[1], Yi Cheng[1], Binbin Liu[1], Xinkui Cheng[1], Hongwei Xi[2]

[1]Department of Orthopedics, Children's Hospital Affiliated to Shanxi Medical University, Taiyuan, People's Republic of China; [2]Department of General Surgery, Children's Hospital Affiliated to Shanxi Medical University, Taiyuan, People's Republic of China; [3]Department of Burn and Plastic Surgery, Children's Hospital affiliated to Shanxi Medical University, Taiyuan, People's Republic of China

Correspondence: Hongwei Xi, Email xihongwei148@sina.com

Background: Multiple stages including hemostasis, inflammation, proliferation, and remodeling were involved in the wound healing process. The increase in nanomaterials in recent years has extended the scope of tools for wound healing; however, it is still difficult to achieve the four multistage procedures simultaneously.

Materials and Methods: In this study, graphene-spiky silica heterostructured nanoparticles (GS) were synthesized for the procedural acceleration of the multistage in wound healing process. The nanobridge effect of GS was analyzed through the adhesion of two skins, the antibacterial effect was assessed in Gram-negative Escherichia coli (*E. coli*) and Gram-positive Staphylococcus aureus (*S. aureus*) bacteria, cell proliferation and migration were investigated in mouse embryonic fibroblast (NIH-3T3) cells, and the in vivo wound healing effect was examined in female BALB/c mice with a cutting wound and *E. coli* or *S. aureus* bacteria infection on the back.

Results: First, GS has a strong nanobridge effect on the rapid closure of wounds because the spiky architecture on the surface of GS facilitates the adhesion of skins, promoting the hemostasis stage. Second, graphene exhibits antimicrobial activities both in chemical and physical interactions, especially under simulated sunlight irradiation. Third, graphene plays an important role in scaffolding function, together with the spiky topographical architecture of GS, accelerating the proliferation and maturation stages.

Conclusion: By periodically promoting every stage of wound healing, GS combined with simulated sunlight irradiation could significantly accelerate wound healing. With a simple composition and compact structure but multiple functions, this strategy will be the guideline for the development of ideal wound-healing nanomaterials.

Keywords: graphene-spiky silica heterostructured nanoparticles, wound healing, multistage

Introduction

Cutaneous wounds have become the main threat to public health and the economy,[1,2] which calls for a deeper understanding of its potential biological mechanisms, and much research effort to develop improved therapeutic approaches. A series of previous studies have shown that multiple stages including hemostasis, inflammation, proliferation, and remodeling were involved in the wound healing process.[3] Hemostasis begins promptly when tissue is damaged and rapid wound closure is required.[4] The main task of the inflammatory stage is to prevent harmful pathogens and bacteria and protect the wound from infection.[5] The proliferation stage mainly involves keratinocytes migration, cellular proliferation, and the formation of new blood vessels (known as angiogenesis).[6] Remodeling as the final stage is characterized by the production of collagen, new epithelium growth, and eventually scar tissue forms.[7] The four stages are carried out in an organized manner to accelerate the whole healing process, otherwise, when various stages in wound healing are not advanced orderly, the entire repair process will be postponed. Recently, the dramatic increase in nanomaterials has extended the scope of tools to accelerate wound healing.[8–12] Various nanomaterials have intrinsic antimicrobial properties originated from their adjustable physicochemical properties or intrinsic biocatalytic activities as nanozymes.[13–24]

Received: 19 July 2023
Accepted: 28 October 2023
Published: 10 November 2023

Moreover, nanomaterials can be used for drug delivery to improve the stability of antibiotic and achieve controlled drug release and targeted bacterial uptake.[25–29] However, the nanosystems works only in some stages and cannot promote the four stages programmatically for effective wound healing. Although some drug-loading systems showed dual action, the synthesis and encapsulation process were complex. Thus, it is necessary to develop intelligent nanosystems that with simple composition, compact structures but can rationally regulate the different stages to accelerate the wound healing process.

Nanoparticles with unique surface architectures exhibit several attractive features for wound healing. In the hemostasis stage, nanoparticles with high surface roughness could match the geometry of tissues to serve as a nanobridge to facilitate the skin adhesion for wound closure, prevent persistent bleeding and fluid loss to accelerate the hemostasis stage.[4,30–34] Moreover, nanoparticles could kill bacteria and quicken the inflammation stage of wound healing through physical and chemical interactions.[35] Among them, graphene nanomaterials have been widely used because of its excellent physical and chemical antibacterial activity.[36] Large surface area and sharp edges contribute to physical damage, which would entrap the bacteria to prevent the nutrients supply to starve the bacteria, and penetrates the bacterial membranes to extract phospholipid molecules destructively, and then damage RNA to exert an antimicrobial effect.[37–41] Chemical damage is caused by oxidative stress or by charge transfer.[42–45] In the proliferation and remodeling stages, extensive research has shown that graphene could act as a scaffold for cell proliferation and migration.[46–49] Furthermore, recent studies have implied that nanotopographical substrate[50] or spiky topographical architecture[33,51] also contribute to cell proliferation and migration. Therefore, engineering the surface structure of nanoparticles has great potential for accelerating the proliferation and remodeling stages of wound healing.

In this study, GS were designed to promote multiple stages of the wound healing process. Spiky silica was attached to graphene via N-hydroxysuccinimide (NHS)/1-ethyl-3-(3-(dimethylamino)-propyl) carbodiimide (EDC) coupling. After application to the wound area, GS could work as follows: (1) in the hemostasis stage, the spiky surface of GS can potentially induce strong interaction with skin tissue, serve as a nanobridge to facilitate wound closure; (2) with the wound healing process proceeding to the inflammation stage, GS exhibited antimicrobial activity under simulated sunlight irradiation, which generated a large magnitude of ROS due to its localized surface plasmon resonance (LSPR) absorption maximum at 280 nm; (3) with the scaffolding function supplied by graphene and the stimulatory effect on proliferation and migration provided by the spiky topographical architecture of GS, the proliferation and remodeling stages were accelerated. Altogether, GS can accelerate multiple stages of the wound-healing process.

Materials and Methods

Materials

Graphite powder (99.95%, CAS:7782-42-5), tetraethyl orthosilicate (TEOS, 99.9%, CAS: 78-10-4), EDC (98%, CAS: 25952-53-8), NHS (98%, CAS: 6066-82-6), (3-Aminopropyl) triethoxysilane (APTES, 99%, CAS: 919-30-2), sodium hydroxide (NaOH, AR, 96%, CAS: 1310-73-2), ethanol (AR, CAS: 64-17-5) and cyclohexane (AR, 99.5%, CAS: 110-82-7) were purchased from Aladdin. Hexadecyltrimethylammonium bromide (CTAB, CAS: 57-09-0) was purchased from Sigma Aldrich. All the chemicals were used as purchased without further purification. Reagent-grade water was obtained from a Milli-Q water purification system (Millipore, Bedford, MA) in all experiments.

Characterization

Scanning electron microscopy (SEM, Hitachi S-4800-II) and transmission electron microscopy (TEM, FEI Tecnai F20) were used to characterize the morphology. Fourier-transform infrared spectroscopy (FTIR) was performed to observe the structure on a Bruker Vertex 70 FT-IR Spectrometer using a KBr pellet. Zeta potential was measured using a Malvern Nanosizer ZS. Ultraviolet-visible (UV−vis) spectra were recorded on a UH5700 UV-Vis/visible/NIR spectrometer. Skin adhesion was measured using the Shimadzu ASG-X instrument. Sun 2000 Solar Simulator (Abet Technologies) was applied to provide the simulated sunlight.

Synthesis of Spiky Silica Nanoparticles

Spiky silica nanoparticles were prepared using the epitaxial growth method in a biphase reaction system according to literature,[52] where TEOS, CTAB, NaOH, and cyclohexane were used as the silica source, template, catalyst, and oil phase, respectively. First, 1.0 g of CTAB and 0.4 mL of NaOH (0.2 M) were added to 50 mL of water at 60 °C. After stirring for 2 h, 20 mL of TEOS in 80 mL of cyclohexane was added dropwise to the above solution and kept stirred for 48 h. Then the spiky silica nanoparticles were centrifuged and washed with water and ethanol at 10,000 rpm for 5 min. The spiky silica nanoparticles were then dissolved in 30 mL of acetone and refluxed for 3 h to remove CTAB templates. After centrifugation again, the particles were washed with ethanol three times and the achieved spiky silica nanoparticles were dried under vacuum at 45 °C. Amino groups (NH_2) were then introduced into the spiky silica nanoparticles by reaction with APTES. Briefly, 50 μL of APTES was added to 10 mL of spiky silica nanoparticle solution in ethanol (10 mg/mL) with stirring at 80 °C overnight. Subsequently, the amino-functionalized spiky silica nanoparticles were centrifuged, washed with ethanol three times, and dried under vacuum at 45 °C to obtain amino functionalized spiky silica nanoparticles.

Preparation of GS

Graphene was obtained using the Hummers method[53,54] and dispersed in 50 mL ultrapure water (1 mg/mL). Subsequently, 15 mM EDC and 25 mM NHS were added under stirring for overnight at room temperature. An amino-functionalized spiky silica nanoparticle aqueous suspension (1 mg/mL, 50 mL) was added with stirring overnight to attach to the graphene.

Adhesion Tests of Two Skins

Twenty microliters of phosphate buffered saline (PBS) or GS (5 mg/mL) was applied between two pieces of skins (1.5 cm × 2.0 cm) get from BALB/c mice and then pressed with a finger for 30 s. Then Shimadzu ASG-X testing machine was used to pull the two skins at a constant rate of 1 mm/min.

ROS Generation Evaluation After Simulated Sunlight Irradiation

Total ROS and singlet oxygen ($^1O_2$) generation of GS were evaluated by 2′,7′-dichlorodihydrofluorescein diacetate (H2DCFDA) and singlet oxygen sensor green (SOSG).[55] H2DCFDA was hydrolyzed to form 2′,7′-dichlorofluorescein (DCF) working solution. Specifically, 10 μL of the stock solution (1 mg/mL H2DCFDA in ethanol) was mixed with NaOH aqueous solution (0.01 mol/L, 1384 μL) for 30 min in dark condition, and 7000 μL of PBS (10 mmol/L, pH = 7.4) was added. 80 μL of DCF (29 μM) or SOSG (12 μM) working solution in each well in a 96-multiwell black plate were mixed with 20 μL of PBS or GS (500 μg/mL) and irradiated by simulated sunlight (0.1 W/cm^2) for 20 min or not. After 6 h of incubation, DCF and SOSG fluorescence emission spectra (500–600 nm) were recorded with the excitation wavelength of 490 nm or 394 nm.

Antibacterial Evaluation of GS Under Simulated Sunlight Irradiation

A diluted bacterial suspension (10^6 colony forming units (CFUs)/mL) was used for antibacterial assessment and bacterial survival was calculated after recording the optical density at 600 nm ($OD_{600\ nm}$). The bacterial solution was mixed with GS at a final concentration of 100 μg/mL and incubated for 6 h at 37 °C with 220 rpm rotation. To evaluate the effects of simulated sunlight on the antibacterial behavior of GS, the mixture was exposed to simulated sunlight (0.1 W/cm^2) for 20 min and further incubated at 37 °C for 6 h. Control experiments were performed as above but without nanoparticles.

For live/dead staining, after 6 h of incubation, with or without exposure to simulated sunlight, the bacteria were washed with PBS and stained with propidium iodide (PI) and SYTO9 in the dark for 30 min. After washed with PBS, the bacteria were collected by centrifugation and 5–10 μL of the bacterial was moved onto a microscope slide and covered by a coverslip for fluorescence imaging.

For CFUs counting on LB agar plates, after 2 h of incubation, with or without exposure to simulated sunlight, the bacterial suspension was diluted 100-fold with growth medium and 20 μL of which was spread onto the agar LB broth for 24 h incubation.

To observe the morphological changes of the bacteria, after 6 h of incubation, with or without exposure to simulated sunlight, the bacteria were collected by centrifugation, washed with PBS and fixed with 2.5% glutaraldehyde, dehydrated by graded ethanol solutions. Finally, 10 μL of bacteria in 100% ethanol were placed on a silicon glide and imaged using SEM. Prior to imaging, the bacteria were coated with gold using a sputter coater.

Intracellular ROS Evaluation

For intracellular ROS assessment, after 6 h of incubation, with or without exposure to simulated sunlight, the bacteria were washed with PBS three times and stained with H2DCFDA for 30 min in the dark. After washed with PBS, the bacteria were collected by centrifugation and 5–10 μL of the bacterial was moved onto a microscope slide and covered by a coverslip for fluorescence imaging.

Cell Proliferation Evaluation

NIH 3T3 cells were purchased commercially from Shanghai Zhong Qiao Xin Zhou Biotechnology Co., Ltd. (Shanghai, China). NIH 3T3 cells was used to evaluate the cell proliferation ability using the kFluor488-EdU assay according to the manufacturer's instructions. Briefly, 5×10^4 NIH 3T3 cells were seeded in each 24 well plate overnight growth. Then 100 μL of fresh medium containing GS (100 μg/mL) was added and co-incubated with the cells for 24 h. Finally, the cells were incubated with EdU (10 μmol/L) for 2 h, fixed with the click-iT reaction mixture and further incubated with DAPI (1 mg/mL) for 30 min for fluorescence imaging.

Cell Migration Assay

About 1.6×10^6 NIH 3T3 cells were seeded into a 6-well plate. After 24 h of growth, a scratch was made using a sterile 10 μL pipette tip guided by laying a sterilized plastic ruler across the top rim of the plate, and serum-free DMEM containing GS (100 μg/mL) was added and co-incubated with the cells for 24 h with or without exposure to simulated sunlight for bright-field imaging.

Cell Viability Assay

Cell Counting Kit-8 (CCK-8) assay was used to assess the biosafety of GS in NIH 3T3 cells. About 1×10^4 3T3 cells in 100 μL culture medium were cultured in each well of a 96-multiwell plate for 24 h. Then the culture medium was taken out and 100 μL of GS with different concentrations of 6.2, 12.5, 25, 50, and 100 μg/mL were added to incubate for 24 h for CCK-8 assay.

In vivo Wound Healing Effect Evaluation

The in vivo wound healing effect was assessed in healthy female BALB/c mice (20 g, 5 weeks old, purchased from Beijing Vital River Experimental Animal Technology Co., Ltd.). All procedures involving experimental animals were in accordance with protocols approved by the Committee for Shanxi Medical University and were in accordance with the guidelines for the Care and Use of Laboratory Animals (NIH, revised 2011). The animal ethics approval number is SYDL2019012. BALB/c mice were randomly divided into four groups: (A) PBS, (B) light, (C) GS, and (D) GS-Light, with four mice per group. The back of the mice was smeared with depilatory cream to remove fur. After anaesthesia, a dorsal wound (about 1.5 cm) on the back of the mice was obtained through a surgical procedure, and the wound was infected by applying 10 μL of *E. coli* or *S. aureus* bacteria suspension (1×10^8 CFU/mL). 20 μL of PBS or GS (5 mg/mL) were moved onto the edge of the wound, and the two contact edges were put together and pressed for 30 s to test wound closure efficacy. B and D groups were irradiated with simulated sunlight (0.1 W/cm^2) for 20 min. We measure the length of the wound and image the wound on days 0, 2, 4, 6, 8, 10, 12, and 14. On day 14 post-wounding, the mice were sacrificed and the wound specimens were collected for haematoxylin and eosin (H&E) and Masson's trichrome staining.

To confirm the successful construction of the infection model, sterilized cotton swabs were used to collect bacterial samples from the wound at 2 h or 7 days post-infection. Cotton swabs were placed in a sterile saline solution (1 mL). After incubation of *E. coli* or *S. aureus* bacteria on LB agar plates for 24 h at 37 °C, the bacterial colonies were imaged.

Statistical Analysis

All data are expressed as mean ± standard deviation (SD). All values were obtained from at least three independent experiments. Statistical significance was evaluated using two-tailed heteroscedastic Student's t-tests. Differences between groups were considered statistically significant when the *p*-value was less than 0.05.

Results and Discussion

Preparation and Characterization of GS

Graphene (G) was first prepared using the Hummers method,[53,54] SEM (Figure 1A), atomic force microscopy (AFM) (upper right in the SEM image in G, Figure 1A) and TEM (Figure 1B) images of graphene showed flake structures with a thickness of a few layers. Amino-functionalized spiky silica nanoparticles with interior nanospheres and epitaxial nanotubes were synthesized through a single-micelle epitaxial growth approach developed by Zhao et al,[52] in which a biphase reaction system was adopted to regulate the continuous interfacial growth of silica spikes. The SEM (Figure 1A) and TEM (Figure 1B) images of the obtained spiky silica nanoparticles (S) showed a spiky-like morphology of approximately 160 nm (Figure 1C), with spherical mesoporous silica cores of approximately 110 nm (Figure 1D) and separated peripheral silica spikes of approximately 25 nm (Figure 1E). Finally, GS was obtained by reacting the amino groups of the spiky silica nanoparticles with the COOH groups of graphene through NHS/EDC coupling. SEM (Figure 1A) and TEM (Figure 1B) images of the GS showed that the spiky silica nanoparticles were successfully linked to graphene. FTIR analysis (Figure 1F) of these materials also confirmed the successful conjugation of the spiky silica to graphene. The characteristic peak at 1088 cm^{-1} was ascribed to Si-O-Si, 1630 cm^{-1} and 1467 cm^{-1} were assigned to the amine N-H bending band and the internal vibration of amide bond peak, indicating that amino groups has been introduced to the surface of SiO_2. 1730 cm^{-1} peak appearance in G indicated the carboxyl groups on graphene. In the spectrum of GS, new peaks at 3447 and 3383 cm^{-1} were assigned to N–H antisymmetric stretching and symmetric stretching, respectively, indicating the success conjugation of spiky silica and graphene. Zeta potentials (Figure 1G) also confirmed the successful synthesis of GS. UV−vis spectroscopy (Figure 1H) indicated that the adsorption peak was located at 280 nm in the UV region.

Nanobridge Effect of GS

Adhesion of the skin for wound closure is the primary task in the hemostasis stage of wound healing. The nanobridge abilities of G, S, and GS were assessed by monitoring the shear strength of mice skin. Figure 2A reveals that except for PBS, G, S, and GS could conjugate to the skin together. To quantify the adhesive strength, the lap-shear adhesion test was performed. It was found that GS showed the largest resist force, followed by S and G (Figure 2B), indicating that GS has a significant nanobridge ability and that the spiky surface may play a major role. Recent studies have shown that geometry-matching spiky nanoparticles can enhance adhesion for long-term bacterial inhibition[56] and enlarge the contact area to inhibit viral replication of virus.[57–59] Therefore, we speculate that the spiky surface produces a geometry-matching effect when the GS interacts with the tissue, thus showing a nanobridge effect and rapid closure of the wound site, which is beneficial for the hemostasis stage of cutaneous wound healing.

ROS Generation and Antibacterial Activity of GS Under Simulated Sunlight Irradiation

During the inflammation stage, pathogens invade the body and induce wound infection.[60] As a result, bacterial inactivation to prevent wound infection can effectively accelerate the wound healing process. Efficient generation of ROS nanoparticles is beneficial for bacterial inhibition. Previous studies have established that simulated sunlight irradiation of graphene can generate $^1O_2$ and introduce carbon-centered free radicals for light-enhanced antibacterial activities.[44,45,61] Therefore, we assessed the ROS generation ability of GS. Total ROS and $^1O_2$ generation of GS were

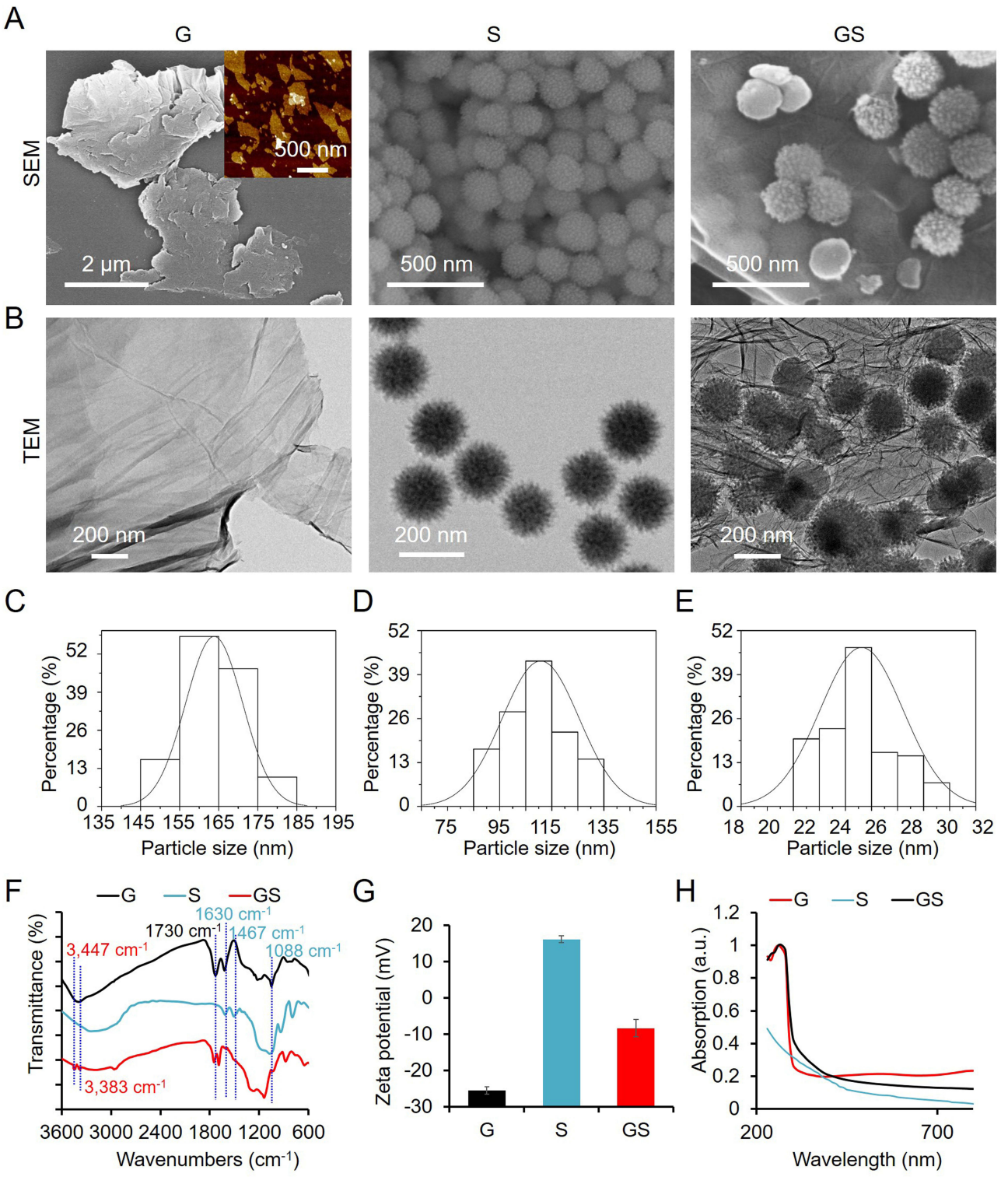

Figure 1 Physicochemical characterization of G, S, and GS. (**A**) SEM images of G, S, and GS. AFM images of G (upper right in the SEM image in (**G**). (**B**) TEM images of G, S, and GS. Size distribution of S (**C**), the spherical mesoporous silica cores (**D**) and the separated peripheral silica spikes (**E**). (**F**) FTIR spectra of G, S, and GS. (**G**) Zeta potential of G, S, and GS. (**H**) UV-vis spectra of G, S, and GS.

evaluated by H2DCFDA and SOSG.[55] Figure 3A and B demonstrate that GS induced more intense DCF and SOSG fluorescence intensities than PBS under simulated sunlight irradiation, indicating the great ROS generation capacity. In comparison, without simulated sunlight irradiation, GS could not generate ROS, as compared to PBS.

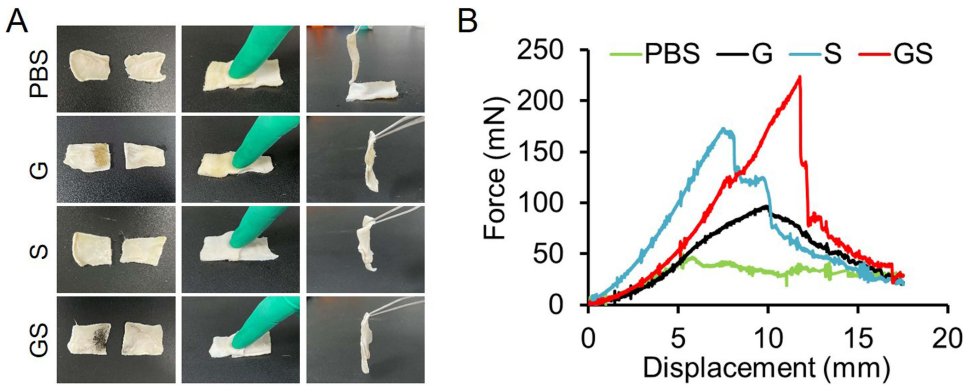

Figure 2 Nanobridge effect of GS. (**A**) Tissue adhesive test of two pieces of mice skins by G, S, and GS. (**B**) Force-displacement curves for lap joints of two skins adhesive by G, S, and GS.

Nanomaterials with abundant ROS generation ability may lead to inactivation of bacteria, as ROS can damage cell membranes, proteins, lipids, and nucleic acids.[62] The antibacterial performance of GS was examined in *E. coli and S. aureus bacteria*. As shown in Figure 3C and D, 20 min of simulated sunlight irradiation alone had negligible effect on *E. coli* and *S. aureus*. GS alone had a survival percentage of 76.2±8.0% and 81.5±0.9% in *E. coli* and *S. aureus*, respectively; However, when irradiated by simulated sunlight, the survival percentage dropped to 31.4±2.6% and 42.2 ±4.6%, implying that the antibacterial activity of GS was significantly enhanced by simulated sunlight. SYTO9 and PI live/dead staining was performed to evaluate the antibacterial activity. As expected, bacteria treated with simulated sunlight or GS alone remained highly viable (green fluorescence), whereas GS and simulated sunlight caused significant apoptosis (red fluorescence) (Figure 3E). Bacterial colony-forming capability was investigated by observing the number of CFUs on LB agar plates after treatment with GS (100 μg/mL) for 6 h. Figure 3F showed that under simulated sunlight irradiation, GS clearly reduced the colony numbers of both *E. coli* and *S. aureus*. Similarly, the CFUs were weakly affected by GS compared with PBS without light irradiation.

Mechanism of the Antibacterial Effect of GS

The excellent ability of GS to produce ROS under simulated sunlight irradiation may have contributed to its prominent antibacterial activity. Thus, the underlying mechanism of the antibacterial activity of GS may be the oxidative stress. ROS levels inside the bacteria were detected using the H2DCFDA assay after treatment with GS for 6 h (100 μg/mL). Figure 4A illustrates that GS with simulated sunlight irradiation could significantly enhance the DCF fluorescence intensities in both *E. coli* and *S. aureus* bacteria compared to PBS, whereas simulated sunlight alone could not trigger DCF fluorescence. This observation suggested an ROS-mediated bacterial inactivation mechanism.

Previous research has established that enhanced adhesion of spiky nanoparticles was beneficial to long-term bacterial inhibition,[56] while graphene can exhibit antibacterial performance through physical damage due to its large surface area and sharp edges.[37–41] The morphologies of *E. coli* and *S. aureus* after treatment with GS were investigated by SEM. As shown in Figure 4B, *E. coli* treated with PBS-or simulated sunlight alone were typically rod-shaped and the cell walls were smooth and intact, whereas GS treatment resulted in the capture of *E. coli* and partial loss of bacterial membrane integrity. However, after exposure to GS with simulated sunlight irradiation, the membrane surface of *E. coli* became rough and wrinkled, causing severe morphological changes and potent antibacterial activity. Similar results were also achieved for *S. aureus* because the smooth and spherical *S. aureus* bacteria became rough and damaged. Overall, these results indicate that GS subjected to simulated sunlight possesses potent antibacterial activity through physical damage and oxidative stress injury, which co-accelerate the inflammatory phase of wound healing by facilitating bacterial inactivation.

Promoting Effects of GS on Cell Proliferation and Migration

Cell proliferation and migration are important in the proliferation and remodeling stages of wound healing. The spiky topographical architecture of the GS is expected to promote cell proliferation[33,50,63,64] and the cell scaffold

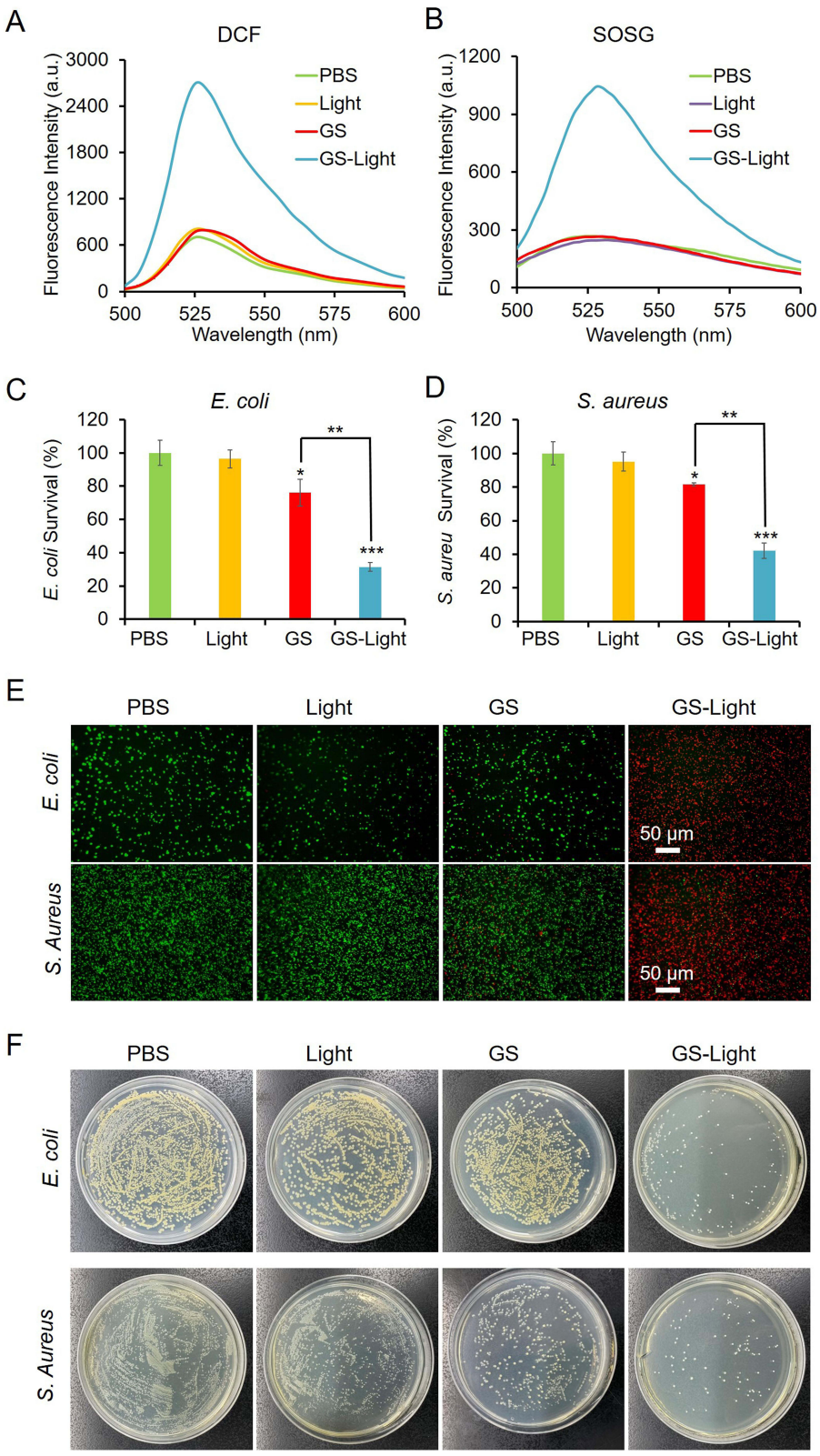

Figure 3 Simulated sunlight-activated ROS generation and antibacterial activity of GS. Total ROS and singlet oxygen-radical generation assessed by DCF (**A**) and SOSG (**B**), respectively, after incubation with GS (100 μg/mL) with or without simulated sunlight irradiation. Bacterial viability of *E. coli* (**C**) and *S. aureus* (**D**) after incubation with GS (100 μg/mL) with or without simulated sunlight irradiation. (**E**) Representative fluorescence images after live–dead fluorescent staining of *E. coli* and *S. aureus* after different treatments. (**F**) Optical images of CFUs forming of *E. coli* and *S. aureus*. *p<0.1, **p<0.01, ***p<0.001.

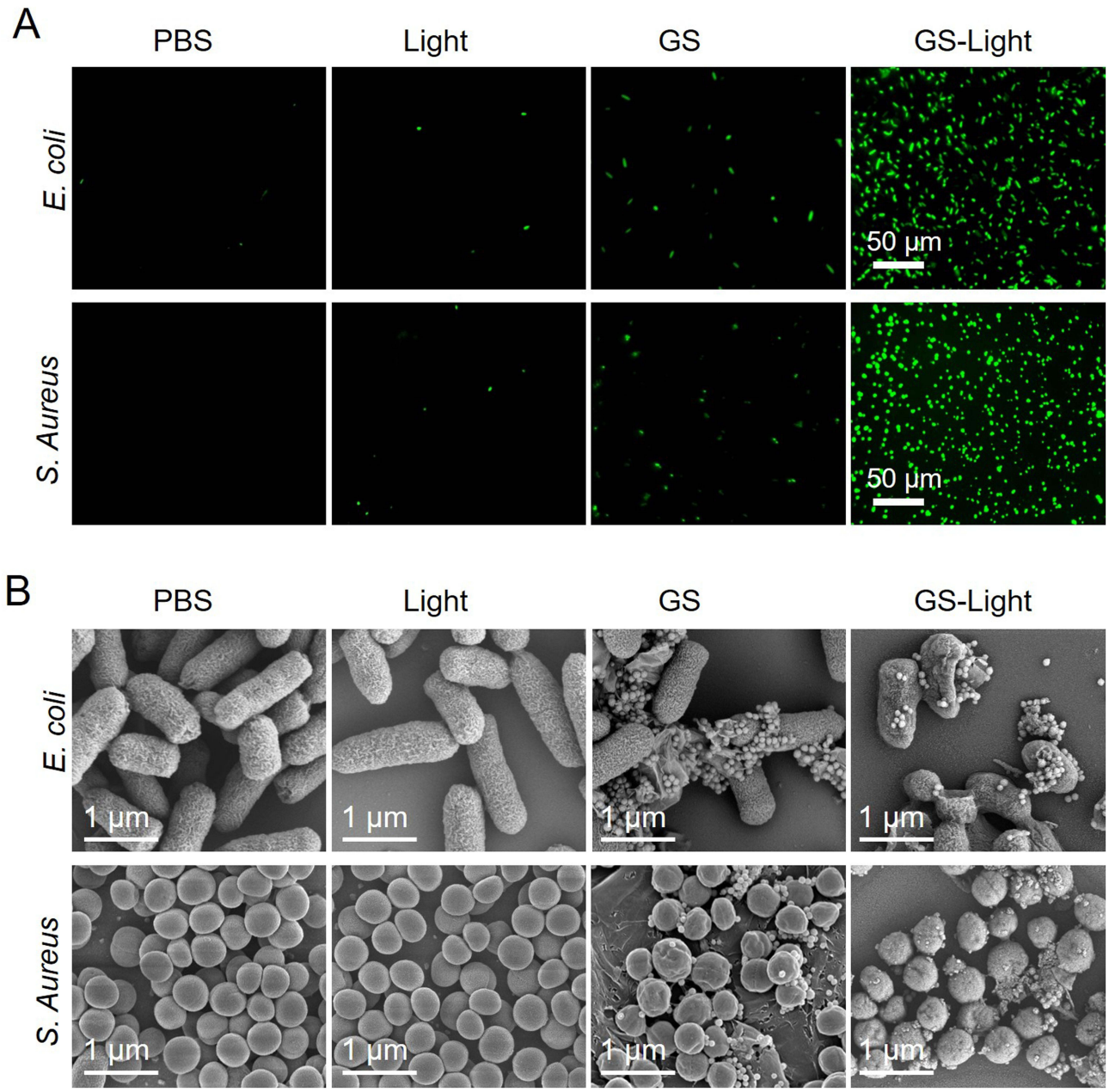

Figure 4 Antibacterial mechanism of GS. (**A**) ROS generation ability of *E. coli* and *S. aureus* incubated with GS with or without simulated sunlight irradiation. (**B**) SEM images of *E. coli* and *S. aureus* after treatment with GS with or without simulated sunlight irradiation. PBS was used as a control.

property of graphene is expected to promote cell migration.[65] Therefore, the proliferative ability of GS was evaluated using the EdU assay in NIH-3T3 cells. Figure 5A displays that 3T3 cells treated with GS exhibited more EdU-positive cells than those treated with PBS or light alone, implying that GS promoted cell proliferation. A time-dependent (0 h, 24 h and 48 h) scratch assay was performed to monitor the cell migration ability of GS (Figure 5B and C). 3T3 cells treated with GS showed more significant migration into the blank region (outlined) than those treated with PBS or light alone at 24 h. After 48 h treatment, GS could promote cell migration completely. These results indicate that GS can significantly promote cell proliferation and migration, potentially accelerating the proliferation and remodeling stages. Cell migration assay showing that GBT significantly increased the migration of NIH-3T3 cells. Then, the biosafety of GS was assessed using CCK-8 assay after 24-h incubation.

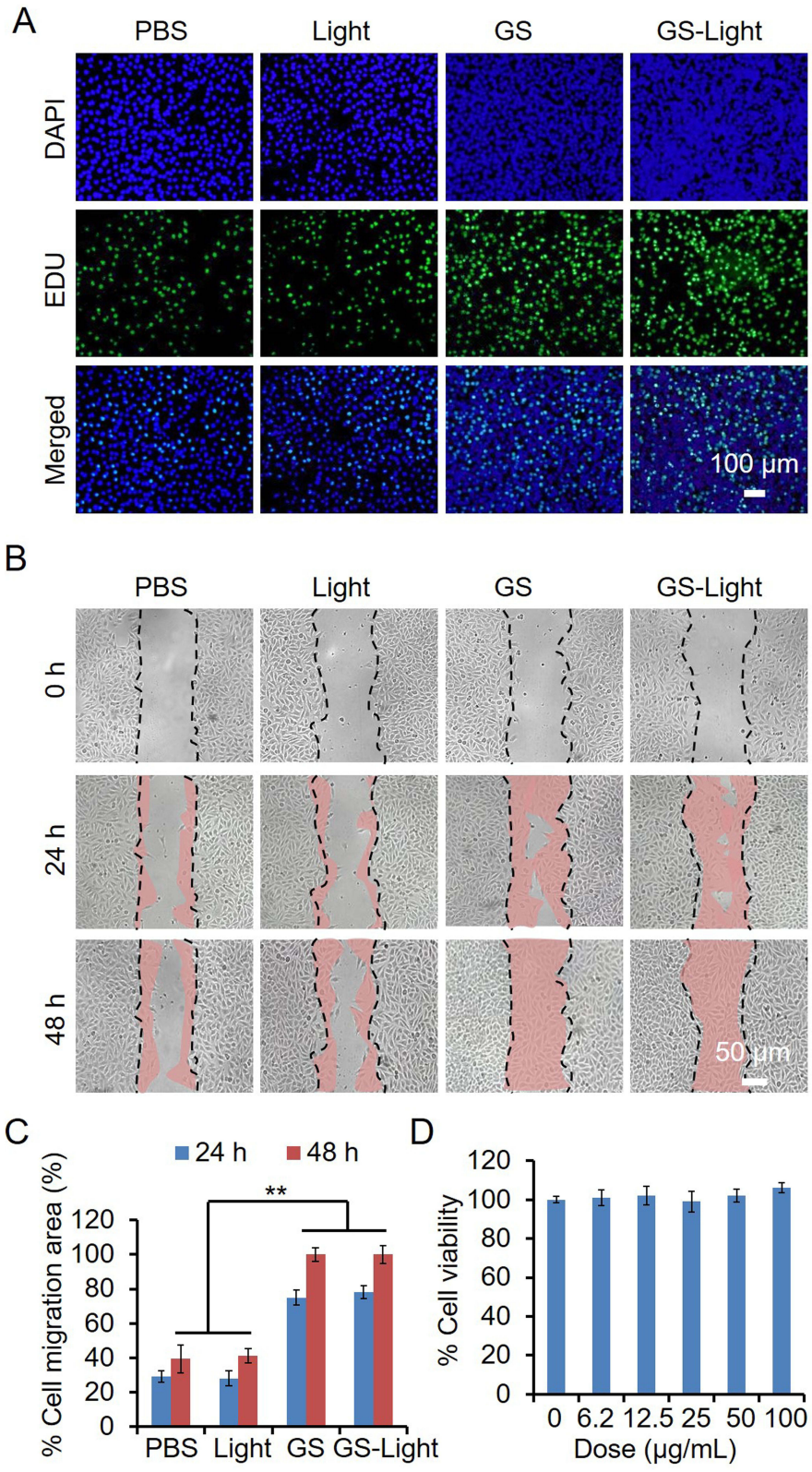

Figure 5 Cell proliferation and migration-promoting abilities of GS. (**A**) Representative fluorescence images of 3T3 cells with EdU-staining (green) and DAPI-staining (blue) after treated with GS with or without simulated sunlight irradiation. (**B**) Scratch wound healing assay after treatment with GS with or without simulated sunlight irradiation at 0 h, 24h and 48 h. (**C**) The Percentage of cell migration area after 24 h and 48 h after different treatment by ImageJ analysis software $^{**}p < 0.01$. (**D**) Cell viability of NIH-3T3 cells treated with GS for 24 h assessed by CCK8 assay.

Figure 5D indicated that cell viability of NIH-3T3 cells was not significantly affected by GS, suggesting the good biosafety of GS for the following in vivo test.

In vivo Wound Healing

Encouraged by the effective wound closure, antibacterial, cell proliferation, and migration abilities of GS, the effectiveness of GS for in vivo wound healing was examined. A cutting wound was created on the backs of the female BALB/c mice. After smearing with *E. coli or S. aureus bacteria* solution at the wound site, infected wounded mice were used as in vivo models. The nanobridging effect was first examined by dropping 20 μL of PBS and GS (5 mg/mL) at the wound and pinching the wound with fingers for 30s. As demonstrated in Figure 6A, GS was very

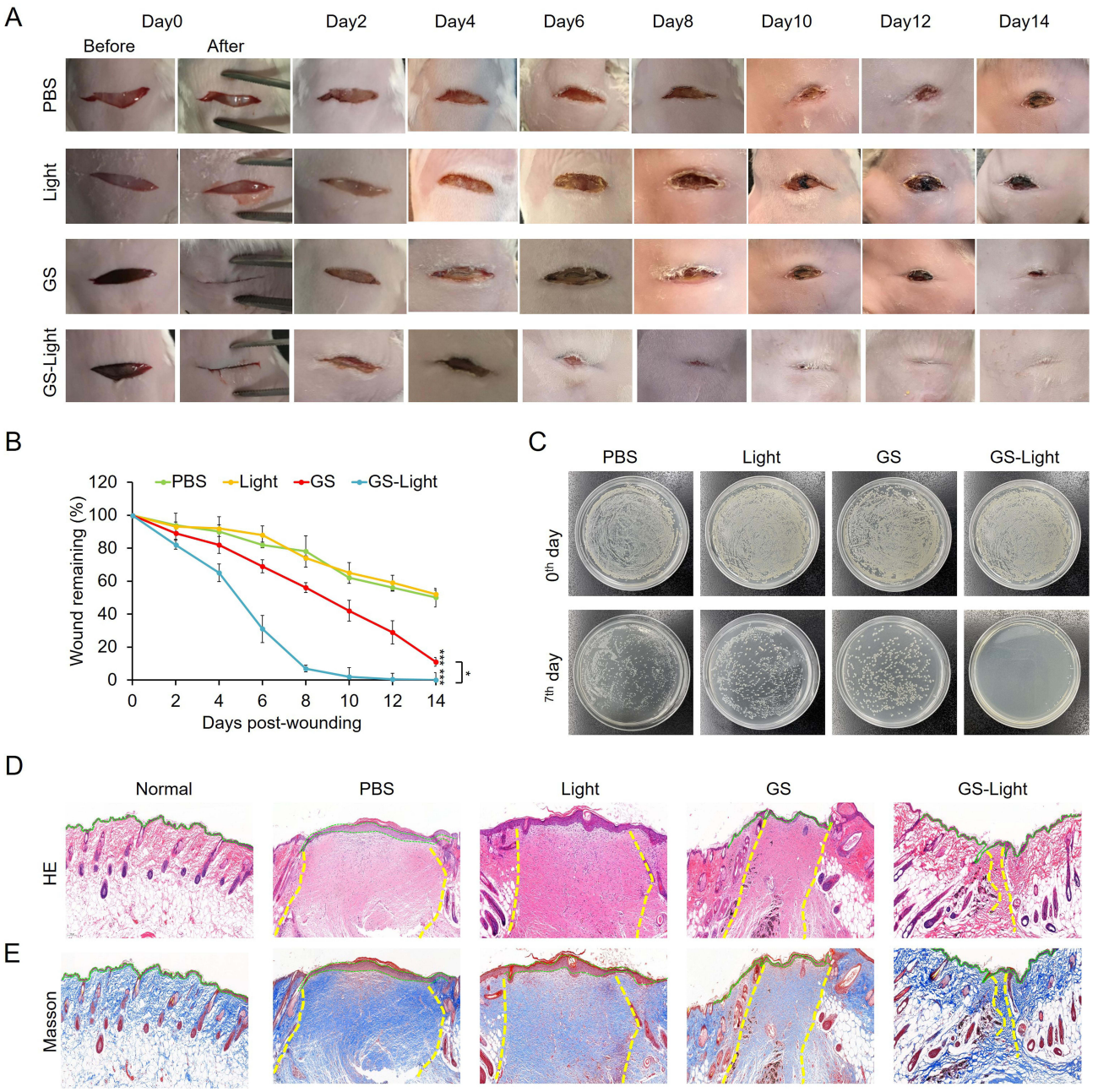

Figure 6 In vivo wound healing performance of GS in *E. coli*-infected wounds. (**A**) Wound images on days 0, 2, 4, 6, 8, 10, 12, and 14. (**B**) Quantification of wound areas as a percentage of the initial wound (n = 5). **p*<0.1, ****p*<0.001. (**C**) Photographs of bacterial colonies collected from *E. coli*-infected wounds at day 0 and day 7. (**D**) H&E and (**E**) Masson's trichrome staining of wound tissues at the end of different treatment; the boundary of the epidermal layer was implied by the green dashed lines, and boundary of the wound area was indicated by the yellow dashed lines.

effective in wound closure, whereas PBS failed (day 0), which was ascribed to the effective nanobridge performance. After irradiation with simulated sunlight for 20 min, the wound sizes were measured and the wound was imaged every 2 days. It was observed that GS treated wounds exhibited a smooth appearance, while wounds treated with PBS or light alone have irregular reddish surface, indicating an excellent healing effect of GS (Figure 6A). Moreover, additional simulated sunlight irradiation could further speed up the wound healing process of GS, which was ascribed to the simulated sunlight-mediated ROS generation that improved the antibacterial activity of GS. Furthermore, the wound area of each group was calculated as the wound-retention curve (Figure 6B), where the wound area treated with GS was dramatically reduced. The antibacterial activity of GS in vivo was confirmed by observing the bacterial

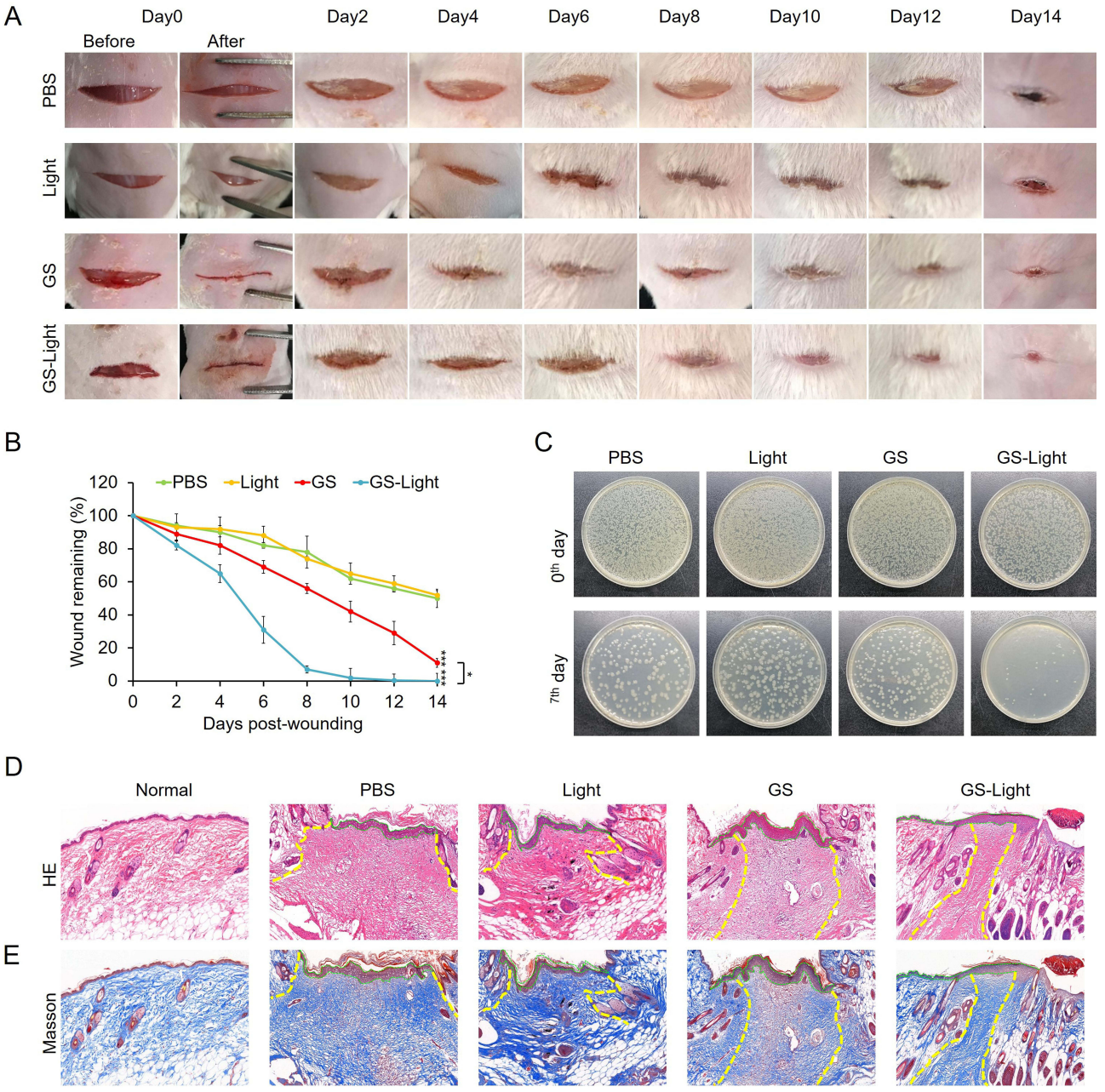

Figure 7 In vivo wound healing performance of GS in *S. aureus* -infected wounds. (**A**) Wound images on days 0, 2, 4, 6, 8, 10, 12, and 14. (**B**) Quantification of wound areas as a percentage of the initial wound (n = 5). **p*<0.1, ****p*<0.001. (**C**) Photographs of bacterial colonies collected from *S. aureus* -infected wounds at day 0 and day 7. (**D**) H&E and (**E**) Masson's trichrome staining of wound tissues at the end of different treatment; the boundary of the epidermal layer was implied by the green dashed lines, and boundary of the wound area was indicated by the yellow dashed lines.

colonies formed. Bacterial colonies were clearly formed on day 0, suggesting the wounds were successfully infected with *E. coli* (Figure 6C, upper). However, after bacteria samples of different groups were collected from the wounds again at day 7 and cultured in vitro, it was found that little bacterial colonies were formed on the culture plate in the GS + Light group (Figure 6C, lower). Although the bacterial colonies were reduced to some degree in the GS group compared to those in the PBS or light groups, the bacterial colonies were clearly visible. These results verify the antibacterial performance of GBT under simulated sunlight irradiation, which can accelerate the wound healing process in vivo. The wound healing-promoting effect of GS was further identified at the histological level. At the end of the 14-day treatment period, skin tissues from the wound areas were harvested for H&E and Masson's trichrome staining. Figure 6D and E show that GS under simulated sunlight irradiation could reduce the scar width effectively (yellow dashed line), and form complete and thickened epidermis (green dashed line), confirming the super wound healing effect of GS under simulated sunlight irradiation.

Similarly, *S. aureus bacteria* infected wound healing process were also investigated. Figure 7A and B implied great nanobridging and wound healing effect of GS. Figure 7C displayed the successful construction of *S. aureus bacteria* infected model (Figure 7C, upper) and the antibacterial effect of GS under simulated sunlight irradiation (Figure 7C, lower), facilitating the whole wound healing process in vivo. H&E (Figure 7D) and Masson's trichrome staining (Figure 7E) were also used to evaluate the internal structure and condition of the healed wounds, revealing similar results as Figure 6D and E. Taken together, the GS was exposed to simulated sunlight irradiation, significantly accelerating wound healing.

Conclusion

Graphene-spiky silica heterostructured nanoparticles were constructed for programmed acceleration of the multistage in wound healing process. GS with a strong nanobridge effect to rapidly close the wounds could promote the hemostasis stage; GS could generate abundant ROS after exposure to the simulated sunlight to promote the inflammation stage; GS could promote proliferation and remodeling stages because of the scaffolding function supplied by graphene and the stimulatory effect provided by the spiky topographical architecture. By periodically promoting every stage of the wound healing stage, GS with simulated sunlight irradiation could accelerate wound healing significantly. With simple composition, compact structures but multiple functions, this strategy will be the guideline for development of new nanomaterials that could accelerate the wound healing process.

Acknowledgments

This work was supported by the Shanxi Province Education Department Foundation (2022L198) and Health Commission of the Shanxi Province Foundation (2021131).

Disclosure

The authors report no conflicts of interest in this work.

References

1. Sen CK. Human Wounds and Its Burden: an Updated Compendium of Estimates. *Adv Wound Care*. 2019;8(2):39–48. doi:10.1089/wound.2019.0946
2. Lo ZJ, Lim X, Eng D, et al. Clinical and economic burden of wound care in the tropics: a 5-year institutional population health review. *Int Wound J*. 2020;17(3):790–803. doi:10.1111/iwj.13333
3. Gurtner GC, Werner S, Barrandon Y, Longaker MT. Wound repair and regeneration. *Nature*. 2008;453(7193):314–321. doi:10.1038/nature07039
4. Meddahi-Pellé A, Legrand A, Marcellan A, Louedec L, Letourneur D, Leibler L. Organ Repair, Hemostasis, and In Vivo Bonding of Medical Devices by Aqueous Solutions of Nanoparticles. *Angew Chem Int Ed*. 2014;53(25):6369–6373. doi:10.1002/anie.201401043
5. Parani M, Lokhande G, Singh A, Gaharwar AK. Engineered Nanomaterials for Infection Control and Healing Acute and Chronic Wounds. *ACS Appl Mater Interfaces*. 2016;8(16):10049–10069. doi:10.1021/acsami.6b00291
6. Werner S, Grose R. Regulation of wound healing by growth factors and cytokines. *Physiol Rev*. 2003;83(3):835–870. doi:10.1152/physrev.2003.83.3.835
7. El Ayadi A, Jay JW, Prasai A. Current Approaches Targeting the Wound Healing Phases to Attenuate Fibrosis and Scarring. *Int J Mol Sci*. 2020;21(3):1105. doi:10.3390/ijms21031105
8. Pérez-Díaz MA, Prado-Prone G, Díaz-Ballesteros A, González-Torres M, Silva-Bermudez P, Sánchez-Sánchez R. Nanoparticle and nanomaterial involvement during the wound healing process: an update in the field. *J Nanopart Res*. 2023;25(2):27. doi:10.1007/s11051-023-05675-9

9. Rajendran NK, Kumar SSD, Houreld NN, Abrahamse H. A review on nanoparticle based treatment for wound healing. *J Drug Delivery Sci Technol*. 2018;44:421–430. doi:10.1016/j.jddst.2018.01.009
10. Barroso A, Mestre H, Ascenso A, Simões S, Reis C. Nanomaterials in wound healing: from material sciences to wound healing applications. *Nano Select*. 2020;1(5):443–460. doi:10.1002/nano.202000055
11. Hu X, Zhang H, Wang Y, et al. Synergistic antibacterial strategy based on photodynamic therapy: progress and perspectives. *Chem Eng J*. 2022;450:138129. doi:10.1016/j.cej.2022.138129
12. Zhao X, Zhang W, Fan J, Chen X, Wang X. Application of mesenchymal stem cell exosomes in the treatment of skin wounds. *Smart Materials Med*. 2023;4:578–589. doi:10.1016/j.smaim.2023.04.006
13. Wei M, Wu J, Sun H, et al. An Enzymatic Antibiotic Adjuvant Modulates the Infectious Microenvironment to Overcome Antimicrobial Resistance of Pathogens. *Small*. 2023;19(4):2205471. doi:10.1002/smll.202205471
14. Liu H, Liu X, Wang H, Ren J, Qu X. A Homing Missile-Like Nanotherapeutic with Single-Atom Catalytic Sites for In Situ Elimination of Intracellular Bacterial Pathogens. *Small*. 2023;19(37):2207510. doi:10.1002/smll.202207510
15. Wu H, Wei M, Hu S, et al. A Photomodulable Bacteriophage-Spike Nanozyme Enables Dually Enhanced Biofilm Penetration and Bacterial Capture for Photothermal-Boosted Catalytic Therapy of MRSA Infections. *Adv Sci*. 2023;10(24):2301694. doi:10.1002/advs.202301694
16. Yi J, Deng Q, Liu Z, et al. Nanozyme-Based Supramolecular Self-Assembly As an Artificial Host Defense System For Treatment of Bacterial Infections. *Small*. 2023;19(32):2301096. doi:10.1002/smll.202301096
17. Jin L, Cao F, Gao Y, et al. Microenvironment-Activated Nanozyme-Armed Bacteriophages Efficiently Combat Bacterial Infection. *Adv Mater*. 2023;35(30):2301349. doi:10.1002/adma.202301349
18. Ma Y, Jiang K, Chen H, et al. Liquid exfoliation of V8C7 nanodots as peroxidase-like nanozymes for photothermal-catalytic synergistic antibacterial treatment. *Acta Biomater*. 2022;149:359–372. doi:10.1016/j.actbio.2022.06.031
19. Wang X, Shi Q, Zha Z, et al. Copper single-atom catalysts with photothermal performance and enhanced nanozyme activity for bacteria-infected wound therapy. *Bioact Mater*. 2021;6(12):4389–4401. doi:10.1016/j.bioactmat.2021.04.024
20. Wang X, Fan L, Cheng L, et al. Biodegradable Nickel Disulfide Nanozymes with GSH-Depleting Function for High-Efficiency Photothermal-Catalytic Antibacterial Therapy. *iScience*. 2020;23:101281.
21. Wu K, Zhu D, Dai X, et al. Bimetallic oxide Cu1.5Mn1.5O4 cage-like frame nanospheres with triple enzyme-like activities for bacterial-infected wound therapy. *Nano Today*. 2022;43:101380. doi:10.1016/j.nantod.2022.101380
22. Zhang W, Dai X, Jin X, et al. Promotion of wound healing by a thermosensitive and sprayable hydrogel with nanozyme activity and anti-inflammatory properties. *Smart Materials Med*. 2023;4:134–145. doi:10.1016/j.smaim.2022.08.004
23. Tian H, Yan J, Zhang W, et al. Cu-GA-coordination polymer nanozymes with triple enzymatic activity for wound disinfection and accelerated wound healing. *Acta Biomater*. 2023;167:449–462. doi:10.1016/j.actbio.2023.05.048
24. Jin X, Zhang W, Shan J, et al. Thermosensitive Hydrogel Loaded with Nickel–Copper Bimetallic Hollow Nanospheres with SOD and CAT Enzymatic-Like Activity Promotes Acute Wound Healing. *ACS Appl Mater Interfaces*. 2022;14(45):50677–50691. doi:10.1021/acsami.2c17242
25. T-T L, Sun L, Zhong Y, et al. Silk fibroin/polycaprolactone-polyvinyl alcohol directional moisture transport composite film loaded with antibacterial drug-loading microspheres for wound dressing materials. *Int J Biol Macromol*. 2022;207:580–591. doi:10.1016/j.ijbiomac.2022.02.105
26. Makabenta JMV, Nabawy A, C-H L, Schmidt-Malan S, Patel R, Rotello VM. Nanomaterial-based therapeutics for antibiotic-resistant bacterial infections. *Nat Rev Microbiol*. 2021;19(1):23–36. doi:10.1038/s41579-020-0420-1
27. Zhang Y, Li -T-T, Wang Z, Shiu B-C, Lin J-H, Lou C-W. Coaxial microfluidic spinning design produced high strength alginate membranes for antibacterial activity and drug release. *Int J Biol Macromol*. 2023;243:124956. doi:10.1016/j.ijbiomac.2023.124956
28. T-T L, Sun L, Zhang Y, et al. Chitosan-based antibacterial microspheres loaded multifunctional Janus composite membranes with unidirectional biofluid transport, antioxidant and pH-responsive monitoring. *Chem Eng J*. 2023;472:144820. doi:10.1016/j.cej.2023.144820
29. Zhang Y, Li -T-T, Shiu B-C, Lin J-H, Lou C-W. Multifunctional sodium Alginate@ urushiol fiber with targeted Antibacterial, acid corrosion resistance and flame retardant properties for personal protection based on wet spinning. *Appl Surf Sci*. 2022;584:152573. doi:10.1016/j.apsusc.2022.152573
30. Wu H, Li F, Wang S, et al. Ceria nanocrystals decorated mesoporous silica nanoparticle based ROS-scavenging tissue adhesive for highly efficient regenerative wound healing. *Biomaterials*. 2018;151:66–77. doi:10.1016/j.biomaterials.2017.10.018
31. Rose S, Prevoteau A, Elzière P, Hourdet D, Marcellan A, Leibler L. Nanoparticle solutions as adhesives for gels and biological tissues. *Nature*. 2014;505(7483):382–385. doi:10.1038/nature12806
32. Wang L, Hussain Z, Zheng P, et al. A mace-like heterostructural enriched injectable hydrogel composite for on-demand promotion of diabetic wound healing. *J Mater Chem B*. 2023;11(10):2166–2183. doi:10.1039/D2TB02403A
33. Wang Y, Feng Y, Yan J, et al. Spiky Surface Topography of Heterostructured Nanoparticles for Programmable Acceleration of Multistage Wound Healing. *Mater Today Nano*. 2023;23:100351. doi:10.1016/j.mtnano.2023.100351
34. Ma X, Cheng Y, Jian H, et al. Hollow, Rough, and Nitric Oxide-Releasing Cerium Oxide Nanoparticles for Promoting Multiple Stages of Wound Healing. *Adv Healthcare Mater*. 2019;8(16):1900256. doi:10.1002/adhm.201900256
35. Bhatt S, Pathak R, Punetha VD, Punetha M. Recent advances and mechanism of antimicrobial efficacy of graphene-based materials: a review. *J Mater Sci*. 2023;58(19):7839–7867. doi:10.1007/s10853-023-08534-z
36. Ji H, Sun H, Qu X. Antibacterial applications of graphene-based nanomaterials: recent achievements and challenges. *Adv Drug Delivery Rev*. 2016;105:176–189. doi:10.1016/j.addr.2016.04.009
37. Tu Y, Lv M, Xiu P, et al. Destructive extraction of phospholipids from Escherichia coli membranes by graphene nanosheets. *Nat Nanotechnol*. 2013;8(8):594–601. doi:10.1038/nnano.2013.125
38. Chen J, Peng H, Wang X, Shao F, Yuan Z, Han H. Graphene oxide exhibits broad-spectrum antimicrobial activity against bacterial phytopathogens and fungal conidia by intertwining and membrane perturbation. *Nanoscale*. 2014;6:1879–1889. doi:10.1016/j.jcis.2018.01.110
39. Mao J, Guo R, Yan L-T. Simulation and analysis of cellular internalization pathways and membrane perturbation for graphene nanosheets. *Biomaterials*. 2014;35(23):6069–6077. doi:10.1016/j.biomaterials.2014.03.087
40. Li Y, Yuan H, von Dem Bussche A, et al. Graphene microsheets enter cells through spontaneous membrane penetration at edge asperities and corner sites. *Proc Natl Acad Sci*. 2013;110(30):12295–12300. doi:10.1073/pnas.1222276110

41. Ye S, Shao K, Li Z, et al. Antiviral Activity of Graphene Oxide: how Sharp Edged Structure and Charge Matter. *ACS Appl Mater Interfaces*. 2015;7(38):21571–21579. doi:10.1021/acsami.5b06876
42. Li J, Wang G, Zhu H, et al. Antibacterial activity of large-area monolayer graphene film manipulated by charge transfer. *Sci Rep*. 2014;4(1):4359. doi:10.1038/srep04359
43. Gurunathan S, Han JW, Dayem AA, Eppakayala V, Kim JH. Oxidative stress-mediated antibacterial activity of graphene oxide and reduced graphene oxide in Pseudomonas aeruginosa. *Int J Nanomedicine*. 2012;7:5901–5914. doi:10.2147/IJN.S37397
44. Guo Z, Zhang P, Xie C, et al. Defining the Surface Oxygen Threshold That Switches the Interaction Mode of Graphene Oxide with Bacteria. *ACS nano*. 2023;17(7):6350–6361. doi:10.1021/acsnano.2c10961
45. Chong Y, Ge C, Fang G, et al. Light-Enhanced Antibacterial Activity of Graphene Oxide, Mainly via Accelerated Electron Transfer. *Environ Sci Technol*. 2017;51(17):10154–10161. doi:10.1021/acs.est.7b00663
46. Kim SE, Kim MS, Shin YC, et al. Cell Migration According to Shape of Graphene Oxide Micropatterns. *Micromachines*. 2016;7:186. doi:10.3390/mi7100186
47. Thangavel P, Kannan R, Ramachandran B, Moorthy G, Suguna L, Muthuvijayan V. Development of reduced graphene oxide (rGO)-isabgol nanocomposite dressings for enhanced vascularization and accelerated wound healing in normal and diabetic rats. *J Colloid Interface Sci*. 2018;517:251–264.
48. Lin F, Du F, Huang J, et al. Substrate effect modulates adhesion and proliferation of fibroblast on graphene layer. *Colloids Surf B Biointerfaces*. 2016;146:785–793. doi:10.1016/j.colsurfb.2016.07.008
49. Ryoo SR, Kim YK, Kim MH, Min DH. Behaviors of NIH-3T3 fibroblasts on graphene/carbon nanotubes: proliferation, focal adhesion, and gene transfection studies. *ACS nano*. 2010;4:6587–6598. doi:10.1021/nn1018279
50. Luu TU, Gott SC, Woo BWK, Rao MP, Liu WF. Micro- and Nanopatterned Topographical Cues for Regulating Macrophage Cell Shape and Phenotype. *ACS Appl Mater Interfaces*. 2015;7(51):28665–28672. doi:10.1021/acsami.5b10589
51. Wang L, Hussain Z, Zheng P, et al. A mace-like heterostructural enriched injectable hydrogel composite for on-demand promotion of diabetic wound healing. *J Materials Chem B*. 2023.
52. Wang W, Wang P, Tang X, et al. Facile Synthesis of Uniform Virus-like Mesoporous Silica Nanoparticles for Enhanced Cellular Internalization. *ACS Cent Sci*. 2017;3(8):839–846. doi:10.1021/acscentsci.7b00257
53. Hummers WS, Offeman RE. Preparation of Graphitic Oxide. *J Am Chem Soc*. 1958;80:1339.
54. Yang K, Feng L, Hong H, Cai W, Liu Z. Preparation and functionalization of graphene nanocomposites for biomedical applications. *Nat Protoc*. 2013;8(12):2392–2403. doi:10.1038/nprot.2013.146
55. Feng Y, Chang Y, Sun X, et al. Differential photothermal and photodynamic performance behaviors of gold nanorods, nanoshells and nanocages under identical energy conditions. *Biomater Sci*. 2019;7(4):1448–1462. doi:10.1039/C8BM01122B
56. Song H, Ahmad Nor Y, Yu M, et al. Silica Nanopollens Enhance Adhesion for Long-Term Bacterial Inhibition. *J Am Chem Soc*. 2016;138(20):6455–6462. doi:10.1021/jacs.6b00243
57. Nie C, Ma L, Luo H, Bao J, Cheng C. Spiky nanostructures for virus inhibition and infection prevention. *Smart Materials Med*. 2020;1:48–53. doi:10.1016/j.smaim.2020.07.004
58. Nie C, Stadtmüller M, Yang H, et al. Spiky Nanostructures with Geometry-matching Topography for Virus Inhibition. *Nano Lett*. 2020;20(7):5367–5375. doi:10.1021/acs.nanolett.0c01723
59. Nie C, Parshad B, Bhatia S, et al. Topology-Matching Design of an Influenza-Neutralizing Spiky Nanoparticle-Based Inhibitor with a Dual Mode of Action. *Angew Chem Int Ed*. 2020;59(36):15532–15536. doi:10.1002/anie.202004832
60. Edwards R, Harding KG. Bacteria and wound healing. *Curr Opin Infect Dis*. 2004;17(2):91–96. doi:10.1097/00001432-200404000-00004
61. Zhang P, Guo Z, Chen C, Lynch I. Uncertainties in the antibacterial mechanisms of graphene family materials. *Nano Today*. 2022;43:101436. doi:10.1016/j.nantod.2022.101436
62. Applerot G, Lellouche J, Lipovsky A, et al. Understanding the Antibacterial Mechanism of CuO Nanoparticles: revealing the Route of Induced Oxidative Stress. *Small*. 2012;8(21):3326–3337. doi:10.1002/smll.201200772
63. Xie X, Melosh NA. Fabrication of sub-cell size "spiky" nanoparticles and their interfaces with biological cells. *J Mater Chem B*. 2015;3(26):5155–5160. doi:10.1039/C5TB00452G
64. Li J, Wen J, Li B, et al. Valence State Manipulation of Cerium Oxide Nanoparticles on a Titanium Surface for Modulating Cell Fate and Bone Formation. *Adv Sci*. 2018;5(2):1700678. doi:10.1002/advs.201700678
65. Mukherjee S, Sriram P, Barui AK, et al. Graphene Oxides Show Angiogenic Properties. *Adv Healthcare Mater*. 2015;4(11):1722–1732. doi:10.1002/adhm.201500155